

Memo No. 135

Draft version October 21, 2025 Typeset using IATEX manuscript style in AASTeX631

Measurement Accuracy Requirement of the ngVLA Water Vapor Radiometer system for Atmospheric Phase Correction in Bands 5 & 6

Yoshiharu Asaki,^{1,2} T. K. Sridharan,³ Kyle D. Massingill,⁴ and Brian E. Svoboda⁴

 $^1 Joint\ ALMA\ Observatory,\ Alonso\ de\ C\'ordova\ 3107,\ Vitacura\ 763\ 0355,\ Santiago,\ Chile$

²National Astronomical Observatory of Japan, 2-21-1 Osawa, Mitaka, Tokyo, Japan

³National Radio Astronomy Observatory, 520 Edgemont Rd. Charlottesville, VA 22903, USA

⁴National Radio Astronomy Observatory, 1011 Lopezville Road, Socorro, NM 87801-0387, USA

ABSTRACT

We have conducted a feasibility study on phase correction with 22 GHz Water Vapor Radiometer (WVR) and phase referencing in Bands 5 and 6 of the next-generation Very Large Array (ngVLA). The goal is to clarify the requirements for path length correction accuracy to be delivered by the overall WVR system. In this study, we first estimate the residual path length error with WVR phase correction during the winter season at the ngVLA sites, represented by the VLA site. Next, we derive the requirements for phase correction to satisfy the dynamic range requirements of 32–28 dB in Bands 5–6. We also consider the requirements for interferometric phase stability from the perspective of interferometric coherence. We evaluate the requirements for the WVR system measurement uncertainty, taking into account residual atmospheric phase errors, dynamic range requirements, and interferometric coherence goals. In conclusion, to meet the dynamic range requirements, the accuracy requirement for the WVR path length error estima-

tion at acquisition time intervals of 1-2 s are $\sim 160~\mu m$ for the 90% coherence goal and $\sim 260~\mu m$ for the 80% coherence goal. Finally, we demonstrate the proposed ngVLA phase calibration method through observational simulations. The synthesized CLEAN images prove the excellent performance attainable using a combination of WVR phase correction and phase referencing.

1. INTRODUCTION

Achieving phase correction at the highest frequencies in ngVLA's Bands 5 and 6 in order to fulfill the science goals with small overheads is quite challenging. Unlike in the lower frequency Bands (Sridharan & Bhatnagar 2023), as self-calibration is not the default phase calibration plan for Bands 5 and 6, appropriate phase calibration techniques must be adopted for the highest frequency observations. Although fast switching phase referencing is feasible for ngVLA (Carilli 2015; Hales 2020; Wrobel & Ho 2022) which provides a default calibration strategy, it requires a calibration cycle time of a few tens of seconds or less for effective phase calibration in Band 6. Given the ngVLA antenna slew and settle performance, the short cycle times entail a calibration efficiency of ~ 50% or less, falling well short of the desired on-target observing efficiency goal of 90%. To meet the challenging phase calibration requirements while maintaining high observation efficiency, Water Vapor Radiometer (WVR) phase correction is considered promising (Clarke 2015; Towne 2020). At the Atacama Large Millimetre/submillimetre Array (ALMA), WVR phase correction utilizing the 183 GHz water line has been implemented and is performing quite successfully (Nikolic et al. 2013; Maud et al. 2017; Matsushita et al. 2017).

This memo presents a feasibility study of ngVLA high frequency phase calibration using a WVR system utilizing the 22.235 GHz water line. Section 2 estimates expected residual excess path length errors after corrections using the WVR system. Section 3 reviews the phase calibration requirements from dynamic range and interferometric phase coherence perspectives and the resulting specifications required for the WVR system. We discuss future work needed in Section 4. Finally, our conclusions are presented in Section 5.

2. ESTIMATION OF THE RESIDUAL INTERFEROMETRIC PHASE ERROR AFTER WVR PHASE CORRECTION

2.1. WVR phase correction for wet air

- 2.1.1. Statistical model for calculating interferometric phase errors due to atmospheric phase fluctuations

 Detailed discussions of atmospheric phase fluctuations can be found in Thompson et al. (2017).

 Let us summarize important assumptions in the analysis of interferometric phase errors due to the water vapor in the atmosphere:
 - Atmospheric phase fluctuations are caused by a laminar screen at an altitude of a few kilometers (phase screen model, Tatarski et al. 1961).
 - The randomized refractive index pattern is frozen on the phase screen, which flows with the wind aloft at a constant speed (typically, $v = 10 \text{ m s}^{-1}$) (frozen flow hypothesis, Tatarski et al. 1961).
 - Atmospheric phase fluctuations are primarily caused by the water vapor content, though dry component also contributes to them.

The first two assumptions can undoubtedly be applied at the VLA site (Carilli & Holdaway 1999), taken to be representative of the ngVLA sites. We must be careful to ensure that the last assumption really holds true, especially under dry conditions (low precipitable water vapor (PWV) conditions) such as in the winter. In WVR phase correction, while liquid water content severely affects the measured system noise temperature, it does not contribute to the atmospheric excess path. Therefore, the application of the WVR phase correction is difficult in relatively humid conditions, especially in the summer. Additionally, high frequency observations require low phase root-mean-square (rms) conditions to reduce coherence loss, in other words, stable atmospheric conditions, which are more prevalent in winter. Although good weather conditions for observing at high frequencies may occur during summers, it would be difficult to realize a feasible phase calibration subsystem with high calibration efficiency covering all the seasons at the highest frequency. Therefore, we assume that

the WVR phase correction will only be applied to ngVLA high frequency observations during low humidity conditions, that is, winter.

2.2. Phase calibration with phase referencing

Before looking into the WVR phase calibration system, we present a statistical model of the calibrated interferometric phase error after phase referencing (rms of residual phase referencing phase $\Delta\Phi$). For simplicity, we assume that the positions of the science target source and phase calibrator do not change with time, constantly directed to s_1 and s_2 , respectively. Let us consider that the interferometric phase error of the target $\Phi(t, s_1)$ is calibrated using two temporally neighboring samples of a spatially neighboring phase calibrator's phase, $\Phi(t-t_{\rm cyc}/2, s_2)$ and $\Phi(t+t_{\rm cyc}/2, s_2)$, as follows:

$$\Delta\Phi(t, \mathbf{s}_{1}, \mathbf{s}_{2}, t_{\text{cyc}}) = \Phi(t, \mathbf{s}_{1}) - \frac{1}{2} \left[\Phi(t - t_{\text{cyc}}/2, \mathbf{s}_{2}) + \Phi(t + t_{\text{cyc}}/2, \mathbf{s}_{2}) \right]. \tag{1}$$

Note that phase referencing can calibrate the interferometric phase errors not only from the atmosphere but also positional offsets of station (antenna) coordinate, signal transmission cables, and time standard (Thompson et al. 2017). In this memo we focus on the performance of atmospheric phase calibration. The standard deviation $\sigma_{\Delta\Phi}$ of $\Delta\Phi$ is expressed as follows (Asaki et al. 1996, see also Appendix A):

$$\sigma_{\Delta\Phi}^2 = \frac{1}{t_{\text{obs}}^2} \int_0^{t_{\text{obs}}} (t_{\text{obs}} - \tau) \bar{D}_{\Delta\Phi}(\boldsymbol{B}, \tau, \boldsymbol{\theta}, t_{\text{cyc}}) d\tau, \tag{2}$$

where $\bar{D}_{\Delta\Phi}$ is the temporal structure function (TSF) of the interferometric phase with the baseline vector \boldsymbol{B} , t_{obs} is a long enough observation time compared to t_{cyc} , and $\boldsymbol{\theta} = \boldsymbol{s}_1 - \boldsymbol{s}_2$. From Equation (1), $\bar{D}_{\Delta\Phi}(\boldsymbol{B}, \tau, \boldsymbol{\theta}, t_{\text{cyc}}) = \langle [\Delta\Phi(t + \tau, \boldsymbol{s}_1, \boldsymbol{s}_2, t_{\text{cyc}}) - \Delta\Phi(t, \boldsymbol{s}_1, \boldsymbol{s}_2, t_{\text{cyc}})]^2 \rangle$ is expressed in terms of the TSF of the interferometric phase $\bar{D}_{\Phi}(\boldsymbol{B}, \tau, \boldsymbol{\theta}) = \langle [\Phi(t + \tau, \boldsymbol{s}_1) - \Phi(t, \boldsymbol{s}_2)]^2 \rangle$ as follows (Asaki 1997):

$$\bar{D}_{\Delta\Phi}(\boldsymbol{B}, \tau, \boldsymbol{\theta}, t_{\text{cyc}}) = \frac{1}{4} \left[6\bar{D}_{\Phi}(\boldsymbol{B}, \tau, 0) - 2\bar{D}_{\Phi}(\boldsymbol{B}, \tau + t_{\text{cyc}}/2, \boldsymbol{\theta})) - 2\bar{D}_{\Phi}(\boldsymbol{B}, \tau + t_{\text{cyc}}/2, -\boldsymbol{\theta})) - 2\bar{D}_{\Phi}(\boldsymbol{B}, \tau - t_{\text{cyc}}/2, -\boldsymbol{\theta})) \right]
- 2\bar{D}_{\Phi}(\boldsymbol{B}, \tau - t_{\text{cyc}}/2, \boldsymbol{\theta})) - 2\bar{D}_{\Phi}(\boldsymbol{B}, \tau - t_{\text{cyc}}/2, -\boldsymbol{\theta}))
+ \bar{D}_{\Phi}(\boldsymbol{B}, \tau + t_{\text{cyc}}, 0) + \bar{D}_{\Phi}(\boldsymbol{B}, \tau - t_{\text{cyc}}, 0)
+ 4\bar{D}_{\Phi}(\boldsymbol{B}, t_{\text{cyc}}/2, \boldsymbol{\theta}) + 4\bar{D}_{\Phi}(\boldsymbol{B}, t_{\text{cyc}}/2, -\boldsymbol{\theta})
- 2\bar{D}_{\Phi}(\boldsymbol{B}, t_{\text{cyc}}, 0) \right].$$
(3)

According to Asaki et al. (1996), \bar{D}_{Φ} is expressed in terms of the spatial structure function (SSF) of a two-element interferometric phase $D_{\Phi}(B) = \langle [\phi(\boldsymbol{x} + \boldsymbol{B}) - \phi(\boldsymbol{x})]^2 \rangle$ suffering fluctuations due to the atmosphere as follows:

$$\bar{D}_{\Phi}(\boldsymbol{B}, \tau, \boldsymbol{\theta}) = 2D_{\Phi}(|\boldsymbol{v}\tau + \boldsymbol{d}_{\theta}|) - D_{\Phi}(|\boldsymbol{v}\tau + \boldsymbol{d}_{\theta} - \boldsymbol{B}|) - D_{\Phi}(|\boldsymbol{v}\tau + \boldsymbol{d}_{\theta} + \boldsymbol{B}|) + 2D_{\Phi}(\boldsymbol{B}), \quad (4)$$

where $\phi(\boldsymbol{x})$ is the line-of-sight excess path length due to the water vapor measured at a single antenna position \boldsymbol{x} , \boldsymbol{v} is the velocity of the wind aloft, and \boldsymbol{d}_{θ} is the horizontal distance on the phase screen between the crossing points of \boldsymbol{s}_1 and \boldsymbol{s}_2 .

To investigate the atmospheric phase error of the ngVLA, we obtain the SSF of the atmospheric phase fluctuations at the VLA site based on Butler & Desai (1999). SSF can be expressed as a power law function with a structure coefficient C_n and a structure exponent 2α as follows:

$$D_{\Phi}(B) = C_{\rm n}^2 B^{2\alpha}.\tag{5}$$

Butler & Desai (1999) report the annual phase rms data at the VLA site measured using the Site

Testing Interferometer (STI) with the 300 m baseline length:

$$\sqrt{D_{\Phi}(B)|_{B=300 \text{ m}}} = 0.0265 \text{ (m)} \times \frac{\phi_{\text{rms}}^{\text{STI}}}{360^{\circ}} ,$$
 (6)

where $\phi_{\text{rms}}^{\text{STI}}$ is the phase rms in degrees measured with the STI at a wavelength of 26.5 mm (11.3 GHz). Here, D_{Φ} is expressed in path length. From Equations (5) and (6), we obtain the structure coefficient as follows:

$$C_{\rm n} = 0.0265 \text{ (m)} \times \frac{\phi_{\rm rms}^{\rm STI}}{360^{\circ}} \times \frac{1}{300^{\alpha}}.$$
 (7)

Figure 1 demonstrates the application of our statistical model to estimate the expected phase rms of ngVLA with B=8 km using phase referencing with the cycle times of 30 s and 60 s, over one year, corresponding to Figures 3 and 4 in Carilli (2015), respectively. We note that the wind velocity is obtained as $300/t_{\rm corner}$. The power law index α and $t_{\rm corner}$ used are from Butler & Desai (1999) and the phase screen height is assumed to be 1 km. The calculations are for 116 GHz. Our results are in good agreement with those obtained by Carilli (2015). We also demonstrate that the results for θ of 0° and 2° as shown with continuous and dashed lines, differ very little. This can be understood based on the distance on the phase screen between the target source and the phase calibrator of ~ 45 m for 2° separation. Accordingly, the effect of the separation on the phase rms is limited compared to $vt_{\rm cyc}/2$, the "effective baseline" for phase referencing at $t_{\rm cyc}$ switching, of a few hundred meters.

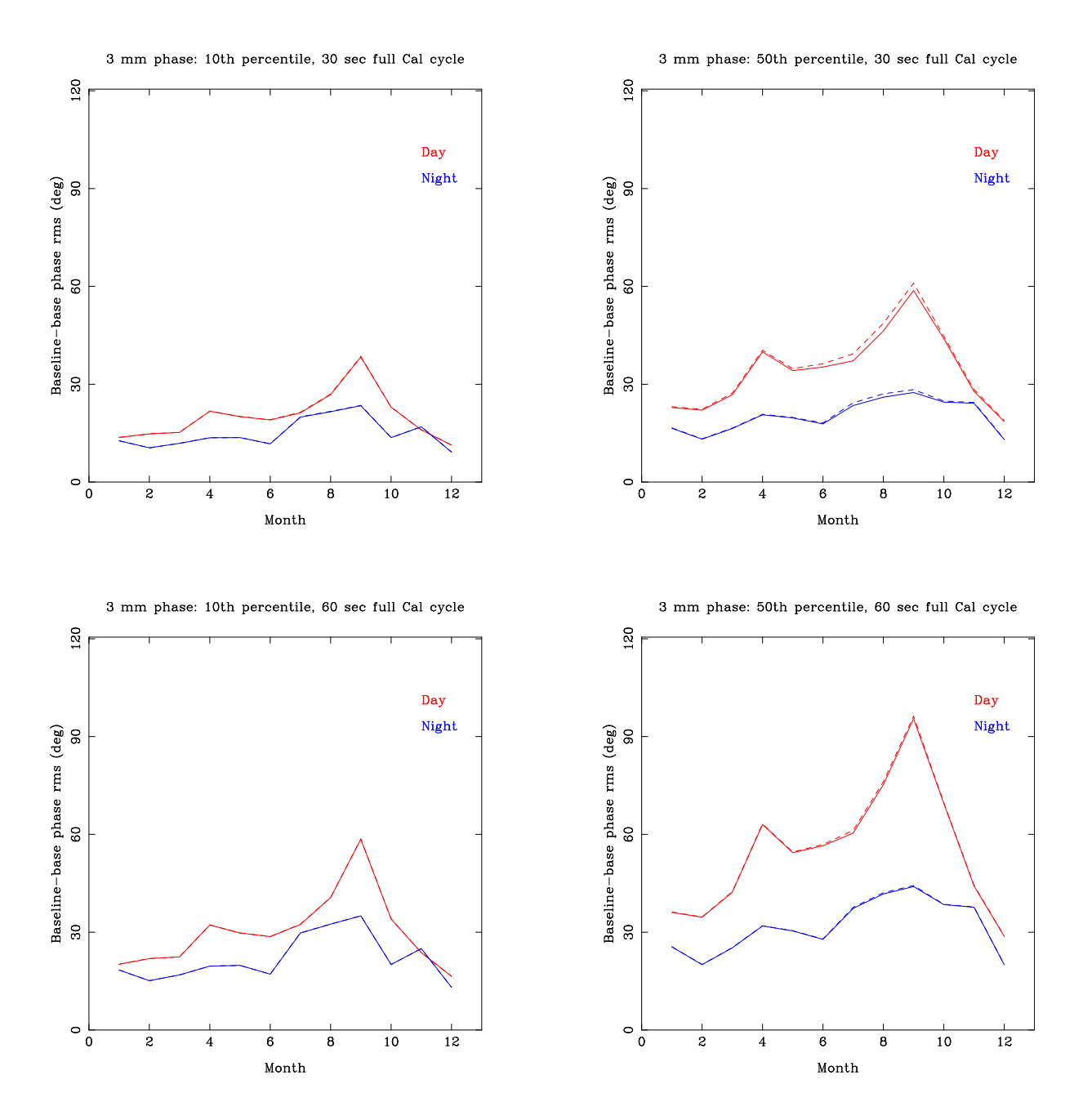


Figure 1. Predicted rms phase noise for a 8 km baseline after phase referencing as a function of month and day/night (red/blue; derived from STI data presented in Butler & Desai (1999)), corresponding to Figures 3 and 4 in Carilli (2015) but with our statistical model described in Sec 2.2. Top: $t_{\rm cyc} = 30$ s, and 10th and 50th percentile conditions are plotted in the left and right plots, respectively. Bottom: $t_{\rm cyc} = 60$ s, and 10th and 50th percentile conditions are plotted. The solid and dashed lines represent the cases with phase calibrator separation angles of 0° and 2° , respectively. The two cases are nearly indistinguishable for the 10th percentile (left panels) and slightly different for the 50th percentile (right panels).

2.3. WVR phase correction for wet air

The statistical model discussed above can be applied to estimate the phase rms of the WVR-corrected phase assuming an ideal WVR system that perfectly tracks the water vapor phase change by observing in the same sky position as the science target. This is equivalent to a phase calibrator $\sim 0^{\circ}$ away being observed simultaneously on a time cadence equal to the WVR acquisition time interval of $t_{\rm wvr}$. The error from a real WVR is discussed later as a separate term in Section 2.5. The primary purpose of this feasibility study is to outline an acceptable tolerance of this error which provides specification requirements of the WVR system.

Let us consider that the interferometric phase error due to the wet air $\Phi_{\rm w}(t, \boldsymbol{s_1})$ is calibrated using two temporally neighboring WVR-derived data samples, $\Phi_{\rm wvr}(t-t_{\rm wvr}/2, \boldsymbol{s_1})$ and $\Phi_{\rm wvr}(t+t_{\rm wvr}/2, \boldsymbol{s_1})$, as follows:

$$\Delta\Phi_{\mathbf{w}}(t, \boldsymbol{s_1}, t_{\mathbf{wvr}}) = \Phi_{\mathbf{w}}(t, \boldsymbol{s_1}) - \frac{1}{2} \left[\Phi_{\mathbf{wvr}} \left(t - t_{\mathbf{wvr}}/2, \boldsymbol{s_1} \right) + \Phi_{\mathbf{wvr}} \left(t + t_{\mathbf{wvr}}/2, \boldsymbol{s_1} \right) \right], \tag{8}$$

where $\Delta\Phi_{\rm w}$ is the WVR-corrected phase. The actual WVR beam may not overlap with the astronomical (science band) antenna beam (e.g., ALMA antenna, Nikolic et al. 2013). In such a case, s_1 in the second and third terms in the right hand of Equation (8) can be replaced to $s_1+\Delta s$. If Δs is small enough, the difference can be negligible (e.g. fast switching with a 2° angle and 30 s cycling; Section 2.2). Assuming that $\Phi_{\rm wvr}$ corresponds to the interferometric phase change due to the water vapor $(\Phi_{\rm wvr}(t, s_1) = \Phi_{\rm w}(t, s_1))$, the standard deviation $\sigma_{\Delta\Phi_{\rm w}}$ of $\Delta\Phi_{\rm w}$ is as follows:

$$\sigma_{\Delta\Phi_{\mathbf{w}}}^{2} = \frac{1}{t_{\text{obs}}^{2}} \int_{0}^{t_{\text{obs}}} (t_{\text{obs}} - \tau) \bar{D}_{\Delta\Phi_{\mathbf{w}}}(\boldsymbol{B}, \tau, t_{\text{wvr}}) d\tau, \tag{9}$$

where $\bar{D}_{\Delta\Phi_{\mathrm{w}}}$ is the TSF of the WVR-corrected interferometric phase:

$$\bar{D}_{\Delta\Phi_{\mathbf{w}}}(\boldsymbol{B}, \tau, t_{\mathbf{wvr}}) = \frac{1}{4} \left[6\bar{D}_{\Phi_{\mathbf{w}}}(\boldsymbol{B}, \tau) - 4\bar{D}_{\Phi_{\mathbf{w}}}(\boldsymbol{B}, \tau + t_{\mathbf{wvr}}/2) - 4\bar{D}_{\Phi_{\mathbf{w}}}(\boldsymbol{B}, \tau - t_{\mathbf{wvr}}/2) \right]$$

$$+\bar{D}_{\Phi_{\mathbf{w}}}(\boldsymbol{B}, \tau + t_{\mathbf{wvr}}) + \bar{D}_{\Phi_{\mathbf{w}}}(\boldsymbol{B}, \tau - t_{\mathbf{wvr}}) - 2\bar{D}_{\Phi_{\mathbf{w}}}(\boldsymbol{B}, t_{\mathbf{wvr}})$$
$$+8\bar{D}_{\Phi_{\mathbf{w}}}(\boldsymbol{B}, t_{\mathbf{wvr}}/2)], \qquad (10)$$

where $\bar{D}_{\Phi_{w}}$ is the TSF of a two-element interferometric phase fluctuation due to the water vapor and expressed in terms of the SSF of the water vapor $D_{\Phi_{w}}(B) = \langle [\phi_{w}(\boldsymbol{x} + \boldsymbol{B}) - \phi_{w}(\boldsymbol{x})]^{2} \rangle$ as follows:

$$\bar{D}_{\Phi_{\mathbf{w}}}(\boldsymbol{B},\tau) = 2D_{\Phi_{\mathbf{w}}}(v\tau) - D_{\Phi_{\mathbf{w}}}(|\boldsymbol{v}\tau - \boldsymbol{B}|) - D_{\Phi_{\mathbf{w}}}(|\boldsymbol{v}\tau + \boldsymbol{B}|) + 2D_{\Phi_{\mathbf{w}}}(B), \tag{11}$$

where $\phi_{\rm w}(\boldsymbol{x})$ is a line-of-sight excess path length due to the water vapor measured at an antenna position \boldsymbol{x} . In the following discussions, we tentatively assume $\bar{D}_{\Phi_{\rm w}}(\boldsymbol{B},\tau) = \bar{D}_{\Phi}(\boldsymbol{B},\tau)$ (i.e. the phase fluctuations are entirely due to water vapor).

Figure 2 shows the standard deviation of the calibrated interferometric phase $\sigma_{\Delta\Phi_{w}}$ (i.e. WVR-corrected) with the statistical model under winter conditions as well as the standard deviation of the uncalibrated interferometric phase. We use the 90th percentile value of α , as presented by Butler & Desai (1999). C_n is then calculated from α and the 90th percentile of ϕ_{rms}^{STI} at night in January and results in 7.76×10^{-6} m^{1- α} with $\alpha = 0.72$. This is taken as typical for winter ngVLA high frequency observations, based on API (Atmospheric Phase Interferometer at the VLA site) rms phase vs. UTC time of day for 18 years at the VLA site (Figures 1-3 in Butler 2020). Note that Carilli (2015) adopted the 50th percentile value of Butler & Desai (1999). In this feasibility study, as the error budget afforded to each error factor has not been addressed yet, we investigate the feasibility somewhat strictly (90th percentile). We have little knowledge of the impact of the dry air component at the ngVLA sites which may be included in a future investigation.

We also assume that the airmass of the present model calculation is the same as that of STI, that is, the observation elevation angle is fixed to $\sim 50^{\circ}$. Note that stepwise SSF power-law exponent changes (e.g., Figure 6 in Carilli & Holdaway 1999) are not considered in the following calculations in order to omit computation cost. Nevertheless, since $t_{\rm wvr}$ is short enough compared to the crossing

time of the phase screen from antenna to antenna, the result would be little different if they are considered.

The top left panel of Figure 2 shows the WVR-corrected phase error $\sigma_{\Delta\Phi_{\rm w}}$, plotted in path length as a function of baseline length for $t_{\rm wvr}$ =1, 2, 4, 6, 10, and 30 s. We adopt a phase screen flow speed of 7.6 m s⁻¹, calculated from $v = 300/t_{\rm corner}$ of the January night 90th percentile condition, parallel to the baseline. The calculation results show that, if the phase fluctuations are caused only by the water vapor content, the WVR-corrected interferometric phase is independent of the baseline length for $B > vt_{\rm wvr}/2$. Specifically, although the figures only show baseline lengths up to 10 km, $\sigma_{\Delta\Phi_{\rm w}}$ remains flat and does not increase for the much longer ngVLA baselines.

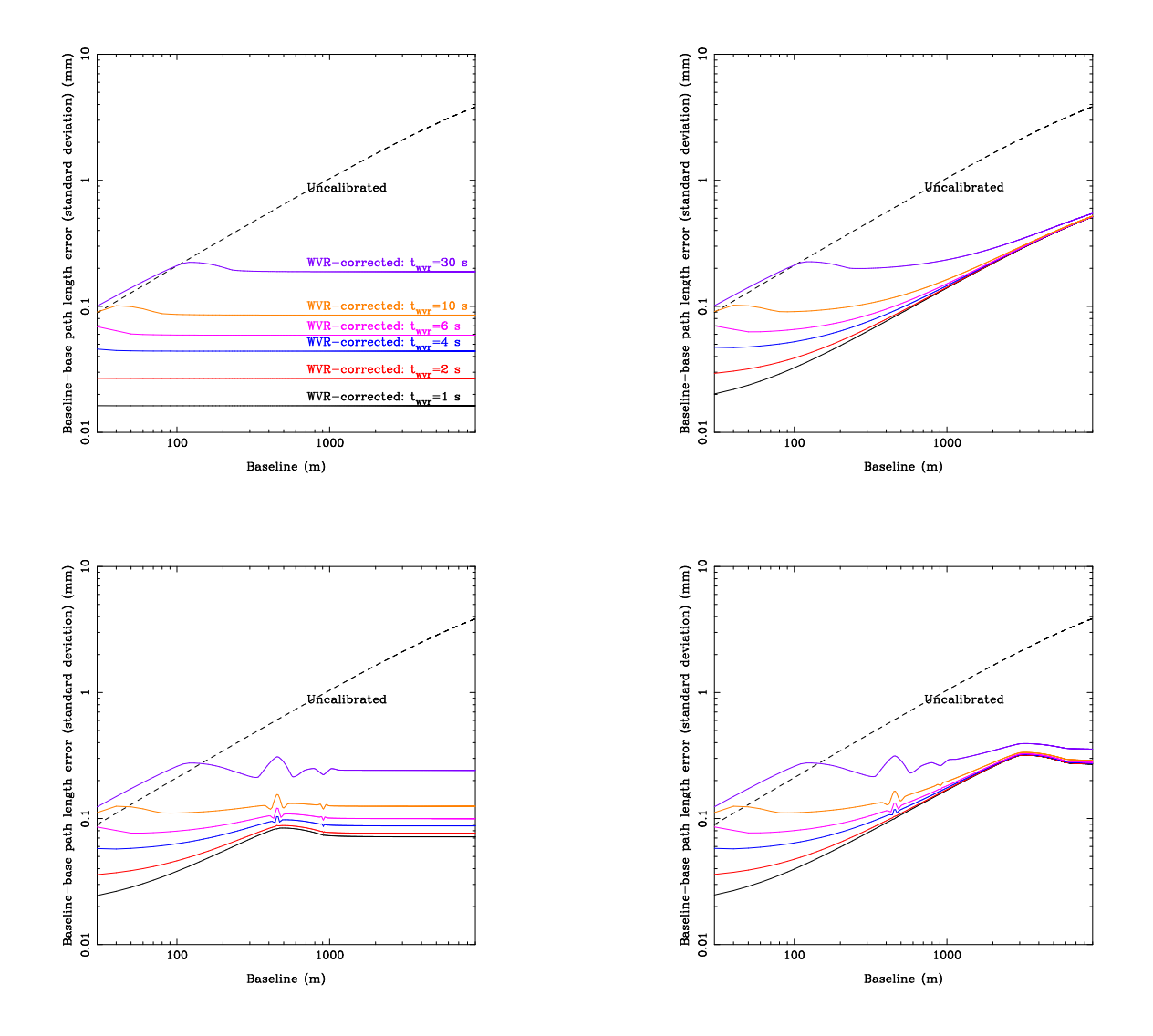


Figure 2. Statistical model calculation of the ngVLA interferometric phase error after WVR phase correction. The horizontal and vertical axes represent the baseline length and standard deviation in path length of a two-element interferometer, respectively. The dashed black lines represent the uncalibrated phase error in path length. The solid black, red, blue, pink, orange, and purple lines represent the WVR-corrected phase error with the WVR acquisition time intervals of 1, 2, 4, 6, 10, and 30 s, respectively. The wet air phase screen flow speed is assumed to be $300/t_{\rm corner}$, parallel to the baseline. Top left: WVR-corrected phase without the dry component phase fluctuations. Top right: WVR-corrected phase with the dry component phase fluctuations (dry component phase screen flow speed of $300/t_{\rm corner}$). Bottom left: WVR and phase referencing corrected phase (120 s cycle time) using a 2° phase calibrator including dry component phase fluctuations with dry component phase screen flow speed of $300/t_{\rm corner}$. Bottom right: the same as the bottom left, but with a dry component phase screen flow speed of 50 m s⁻¹. The weather is assumed to be the January night 90th percentile condition, as presented by Butler & Desai (1999). Note that a stepwise SSF power-law exponent change (e.g., Fig.6 in Carilli & Holdaway 1999) is not considered.

2.4. Dry component contributions to the phase fluctuations

2.4.1. Statistical model for calculating interferometric phase errors due to the dry component

Matsushita et al. (2017) report that while the ALMA 183 GHz WVR is quite successful in suppressing the interferometric phase fluctuations, there are still baseline-dependent phase fluctuations in the WVR-corrected phase. They speculate that the remaining phase fluctuations can be ascribed to the atmospheric dry air components and/or water ice which cannot be sensed by the WVR. We will estimate how non-water-vapor components (hereafter, we call dry component) would affect the phase fluctuations for the ngVLA. According to Maud et al. (2023), the WVR-corrected phase rms with the baseline of 1000 m in the winter season at ALMA is ~ 0.050 mm rms in path length. Matsushita et al. (2017) estimate the averaged SSF power law exponent of the ALMA WVR-corrected phase to be 1.2. With those values, we obtain the structure coefficient of the dry component $C_{\rm n-dry}$ of 0.794×10^{-6} . Since the dry component refractive index is proportional to the atmospheric pressure at the ground surface, we adjust this value to fit to ngVLA by a multiplying factor of 786 hPa (at the VLA site) / 570 hPa (at the ALMA site) and obtain $C_{\rm n-dry} = 1.09 \times 10^{-6}$. The dry component contributes to the phase error as follows:

$$\sigma_{\Phi_{\mathbf{d}}}^2 = \frac{1}{t_{\text{obs}}^2} \int_0^{t_{\text{obs}}} (t_{\text{obs}} - \tau) \bar{D}_{\Phi_{\mathbf{d}}}(\boldsymbol{B}, \tau) d\tau, \tag{12}$$

where $\bar{D}_{\Phi_{\rm d}}$ is the TSF of the dry air component phase fluctuations. The top right panel of Figure 2 shows the residual path length fluctuations as a function of baseline after the WVR phase correction with the dry component phase screen at the flow speed of $300/t_{\rm corner}$, whose SSF is assumed to have the same structure exponent of the water vapor SSF. Although the WVR phase correction dramatically reduces the interferometric phase error, the residual baseline-dependent phase errors due to the dry component are present and increase with the baseline length. This can especially affect long baseline observations. We note that $\sigma_{\Phi_{\rm d}}$ would saturate at the outer scale and remain flat thereafter.

2.4.2. Phase referencing

For ngVLA, the WVR phase correction would not compensate for the dry component of interferometric phase fluctuations, as can be seen with ALMA. If the WVR phase correction is inadequate for phase calibration at longer baselines, as shown in the top right panel of Figure 2, then phase referencing is necessary to mitigate the dry component phase fluctuations. Phase referencing on longer time scales (compared to t_{wvr}) is also required for continuous recalibration of the WVR parameters (e.g. channel weights) of the water vapor excess path estimation algorithm.

Here, we assume adopting phase referencing for the WVR-corrected phases with the 120 s cycle time, which would result in a calibration efficiency of $\sim 80\%$. Note that such phase referencing barely affects the WVR phase correction (except aiding with WVR algorithm parameter updates). After phase referencing, the dry component phase error, $\sigma_{\Delta\Phi_d}$, is expressed as follows:

$$\sigma_{\Delta\Phi_{\rm d}}^2 = \frac{1}{t_{\rm obs}^2} \int_0^{t_{\rm obs}} (t_{\rm obs} - \tau) \bar{D}_{\Delta\Phi_{\rm d}}(\boldsymbol{B}, \tau, t_{\rm cyc}) d\tau, \tag{13}$$

where $\bar{D}_{\Delta\Phi_{\rm d}}$ is the TSF of the phase-referenced dry component phase fluctuations. The statistical model calculation results for WVR-corrected and phase referenced residual phase is presented in the bottom left panel of Figure 2. For simplicity, we assume the use of a 2° (and quite bright) phase calibrator.

This calculation assumes that the phase screen flow of the dry component is the same as that of the wet component, but we are not confident that this assumption is correct. There may be a possibility that turbulence of the dry component can develop on a larger scale, causing phase fluctuations at a different altitude than the wet component (Asaki et al. 2016). If the dry component phase screen flow is 50 m s⁻¹ instead of $300/t_{\text{corner}}$, the resultant phase error after WVR phase correction and 120 s phase referencing does not depend much on t_{wvr} but depends on the baseline length until 3 km, as shown in the bottom right panel of Figure 2. In such a case, faster phase referencing (and lower calibration efficiency) may be required for high frequency long baseline observations. As noted before,

the residual fluctuations shown in the bottom panels, after WVR and phase referencing corrections, would remain flat for the much longer ngVLA baselines not plotted. In future high frequency phase calibration studies, it is important to analyze not only water vapor phase fluctuations but also dry component phase fluctuations. In this memo, we assume, rather optimistically, that the dry component phase fluctuations are caused at the same altitude as the wet component and that the phase screen flows at the same speed as the wet component.

2.5. WVR system error and measurement accuracy requirements

A prospective ngVLA WVR tropospheric phase correction system would nominally equip each element antenna with a WVR instrument. If we consider the WVR system measurement error at each station to be $\sigma_{\rm wvr}$, the total sum of errors must be below the required measurement accuracy (Section 3). For corrections applied to interferometric phase per baseline, the error would be $\sqrt{2}\sigma_{\rm wvr}$. In interpolating a value at the center of two temporally independent measurement points, the error is transferred from the two measurements so that the dispersion at the inserted point has a variance of $(2\sigma_{\rm wvr}^2)/2$. Therefore, a tolerable total phase error per baseline $\sigma_{\rm req}$ satisfying dynamic range requirement, interferometric coherence goal, etc., described in the next Section is expressed as follows:

$$\sigma_{\text{req}}^2 \geq \sigma_{\Delta\Phi_{\text{w}}}^2 + \sigma_{\Delta\Phi_{\text{d}}}^2 + \sigma_{\text{wvr}}^2,$$
 (14)

or

$$\sigma_{\text{wvr}} \leq \sqrt{\sigma_{\text{req}}^2 - \sigma_{\Delta\Phi_{\text{w}}}^2 - \sigma_{\Delta\Phi_{\text{d}}}^2}$$
 (15)

3. REQUIRED INTERFEROMETRIC PHASE STABILITY (PATH LENGTH STABILITY)

3.1. Dynamic range requirement

The dynamic range of an ngVLA observation can be expressed as follows (Sridharan & Bhatnagar 2023):

$$DR \sim \frac{\sqrt{N} \times \sqrt{M}}{\phi_{\rm rms}^{\rm cal}} = \frac{\lambda}{\sigma_{L_{\rm DR}}} \frac{\sqrt{N} \times \sqrt{M}}{2\pi}$$
 (16)

where DR is the dynamic range, N is the number of antennas, M is the number of independent "snapshots" (with fluctuation corrections) each with an integration time of $t_{\rm int}$, λ is the observing wavelength, $\phi_{\rm rms}^{\rm cal} = 2\pi\sigma_{\rm L_{DR}}/\lambda$ is rms of the residual phase error after phase correction (calibration), and $\sigma_{\rm L_{DR}}$ is the rms path length error after phase correction. This expression assumes that the residual "snapshots" fluctuation corrections are random with no systematic trends over the longer term of M "snapshots". Any such longer term trends can be calibrated out through ~ 3 min scale phase referencing and self-cal on time scales where sufficient S/N has been accumulated. As the DR requirements have been set to scale with λ (follow 1/f; Selina 2021) and the water vapor delay is non-dispersive, given the same λ scaling in Equation (16) the path length error requirement derived for one frequency would allow the DR requirement to be met at another frequency.

For the ngVLA high frequency Bands, the required DR is 32 dB (=1585) in Band 5 (minimum $\lambda = 5.94$ mm), and 30 dB (=1000) and 28 dB (=631) in Band 6 at 70 GHz ($\lambda = 4.28$ mm) and 116 GHz ($\lambda = 2.58$ mm), respectively, deviating slightly from λ scaling for Band 5 (presumably rounded to whole numbers in dB). To deliver the DR requirement in a short observation without the full array, we assume N is 107 and that the observation time is one hour (3600 s). In this feasibility study, we treat $t_{\rm int}$ as $t_{\rm wyr}$. Then, $\sigma_{\rm L_{DR}}$ shall be as follows:

$$\sigma_{\rm L_{DR}} \text{ (mm)} \le 0.370 \times t_{\rm wvr}^{-0.5} \text{ (at 50.5 GHz in Band 5)},$$
 (17)

$$\sigma_{\rm L_{DR}} \text{ (mm)} \le 0.423 \times t_{\rm wvr}^{-0.5} \text{ (at 70 GHz in Band 6)},$$
 (18)

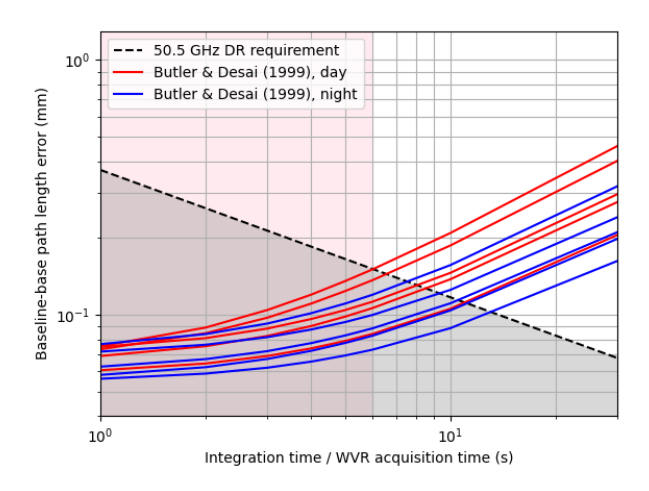
$$\sigma_{\rm L_{DR}} \text{ (mm)} \le 0.404 \times t_{\rm wvr}^{-0.5} \text{ (at 116 GHz in Band 6)}.$$
 (19)

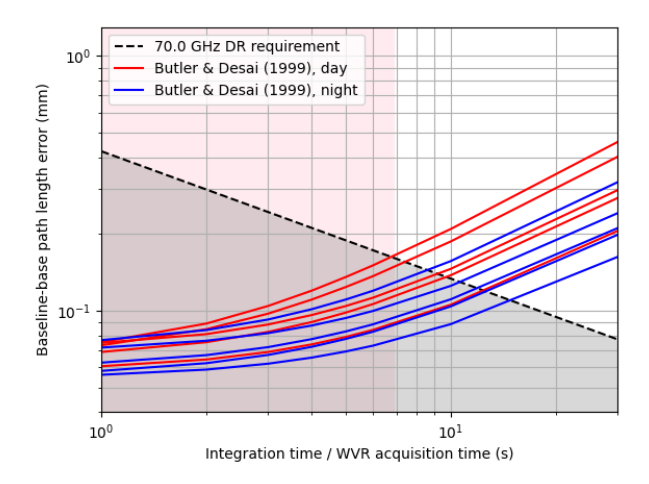
The required path length rms values for $t_{\rm wvr} = 1, 2, 3, 4, 5, 6, 10$, and 30 s are listed in Table 1. The path length rms requirements would have been identical for all frequencies in Bands 5 and 6 with true λ scaling of DR.

Figure 3 plots the $\sigma_{L_{DR}}$ requirements for the above three cases in Bands 5 and 6 (dashed lines which are slightly different) and the phase errors in path length (solid lines) after WVR phase correction and phase referencing with 120 s cycle time for 90th percentile atmospheric conditions presented by Butler & Desai (1999) for the winter season (November to March) and 8-km baseline. As already pointed out and shown in Figure 2, $\sqrt{\sigma_{\Delta\Phi_{\rm w}}^2 + \sigma_{\Delta\Phi_{\rm d}}^2}$ is flat beyond a few km, and this discussion can be applied to longer baseline arrays. Note that this results in a conservative estimates (more stringent) for the time scales derived below, as the fluctuations are smaller for shorter baselines. Since we seek to derive requirements for an antenna based correction system and a given antenna is part of many baselines of various lengths, including long baselines, it is appropriate to use a long baseline length above which the fluctuations do not increase, which provides worst case estimates. To achieve the required dynamic range, the WVR-corrected phase error should remain below the dashed lines: thus, the acquisition time interval must be shorter than ~ 6 s (pink colored area), set by Band 5, for the worst month, daytime. On the other hand, excluding November and March daytime allows for a beneficially wider parameter space for determining the specification: for example, allowable $t_{\rm wvr}$ extends to ~ 8 s. In this memo, we discuss the specification requirements for the worst conditions in the winter season: the WVR acquisition interval time should be shorter than ~ 6 s.

3.2. Interferometric coherence goal

Here, we consider another factor of interferometric phase stability, from a coherence loss perspective. Residual phase errors from the WVR system degrade the coherence of the WVR-corrected interferometric phase, leading to an amplitude loss. If the noise characteristics of the WVR path length estimates are those of Gaussian random noise, the coherence factor, η_c , is calculated as follows





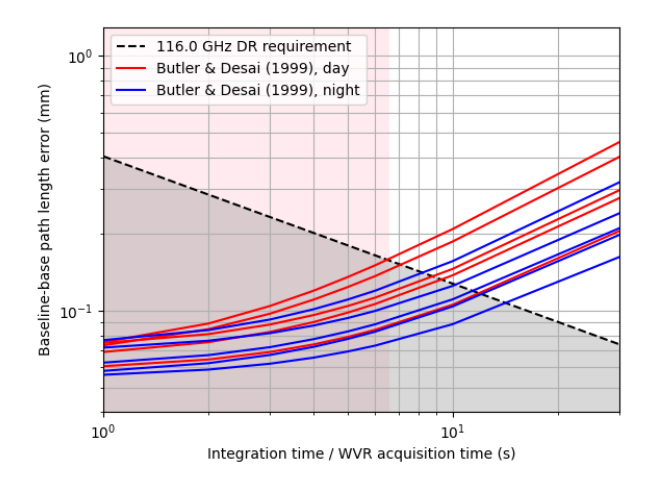


Figure 3. Phase error (standard deviation in path length) versus the WVR acquisition time interval. WVR-corrected phase is assumed to be calibrated using a 2° phase calibrator with the 120 s cycle time phase referencing. The solid lines show the path length error of the WVR-corrected baseline-based interferometric phase, obtained from our statistical model for conditions described in Butler & Desai (1999). The red lines represent daytime data, and the blue lines represent nighttime data, for each month from November to March. The dashed line shows the path length stability required for dynamic range (Sridharan & Bhatnagar 2023) of 32 dB at 50.5 GHz (Band 5), and 30 and 28 dB at 70 GHz and 116 GHz (Band 6) in the top left, top right, and bottom center panels, respectively. The pink colored regions indicate the allowable WVR acquisition time interval so that the residual atmospheric phase error meets the dynamic range requirement for the worst month, daytime.

Table 1. Required path length (and phase) rms in mm (and degree) to achieve the required dynamic range of 32 dB in Band 5, and 30 dB and 28 dB in Band 6 at 70 and 116 GHz, respectively, for WVR sampling time of 1, 2, 3, 4, 5, 6, 10, and 30 s.

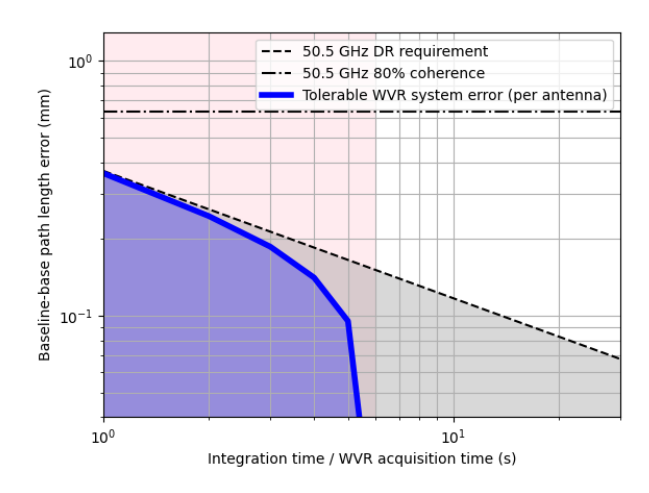
	1 s	2 s	3 s	4 s	5 s	6 s	10 s	30 s
50.5 GHz (Band 5)	0.37 (22)	0.26 (16)	0.21 (13)	0.19 (11)	0.17 (10)	0.15 (9)	0.12 (7)	0.07 (4)
$70~\mathrm{GHz}~(\mathrm{Band}~6)$	0.42 (36)	0.30 (25)	0.24 (21)	0.21 (18)	0.19 (16)	0.17 (15)	0.13 (11)	0.08(6)
116 GHz (Band 6)	0.40 (56)	0.29 (40)	0.23 (33)	0.20 (28)	0.18 (25)	0.17 (23)	0.13 (18)	0.07 (10)

(Thompson et al. 2017, ch. 13.1.6):

$$\eta_{\rm c} = \exp\left(-\frac{\sigma_{\rm \Phi_g}^2}{2}\right) = \exp\left(-\frac{2\pi^2 \sigma_{L_g}^2}{\lambda^2}\right),$$
(20)

where σ_{Φ_g} and σ_{L_g} are the phase and path length errors, which are assumed to be random Gaussian noise.

The ngVLA system level requirements do not specify an allowed coherence loss due to atmospheric phase fluctuations. However, the ngVLA Calibration Concept (Sridharan et al. 2024) provides the guiding stipulation that under unstable atmospheric conditions resulting in a large phase rms at a given frequency, the dynamic scheduling system/operators must move to a lower frequency observation to avoid significant coherence loss. An upper limit for the coherence loss requirement may be set as 1% S/N degradation, if we consider the instrumental delay/phase errors requirement (Selina 2021, SYS1301) to apply to the residual fluctuations after correction by the WVR system. However, this requirement is too strict and infeasible to apply to the coherence loss due to residual atmospheric phase fluctuations after correction in Bands 5 and 6. Allowing the amplitude degradation in Band 6 to be up to 10% and 20% ($\eta_c > 90\%$ and 80%, respectively), σ_{Φ_g} should be less than 0.459 and 0.668 rad rms, respectively. This corresponds to 0.188 and 0.275 mm rms in path length, respectively, at 116 GHz in Band 6, where the impact is the worst. These two coherence goals are plotted



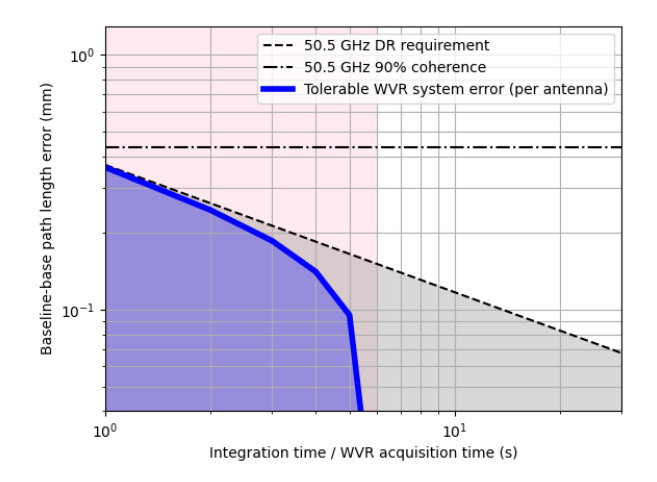


Figure 4. Requirements for path length stability at 50.5 GHz in Band 5 derived from the dynamic range requirement of 32 dB and coherence goals. The dashed line shows the requirement for path length stability to achieve the dynamic range. Dash-dotted lines represent the upper limit of the path length error to achieve coherence of 80% (left panel) and 90% (right panel). The pink colored region is the same as Figure 3. The gray colored region is the allowed WVR system error in path length to meet the dynamic range requirement without considering the coherence loss due to residual atmospheric phase error. The blue colored area is permitted region in the timescale-WVR system error parameter space, as calculated by Equation (15), for November daytime observations (the worst case).

in Figures 4, 5, and 6 as black dashed horizontal lines for the three cases at 50.5 GHz (Band 5), 70 and 116 GHz (Band 6), respectively.

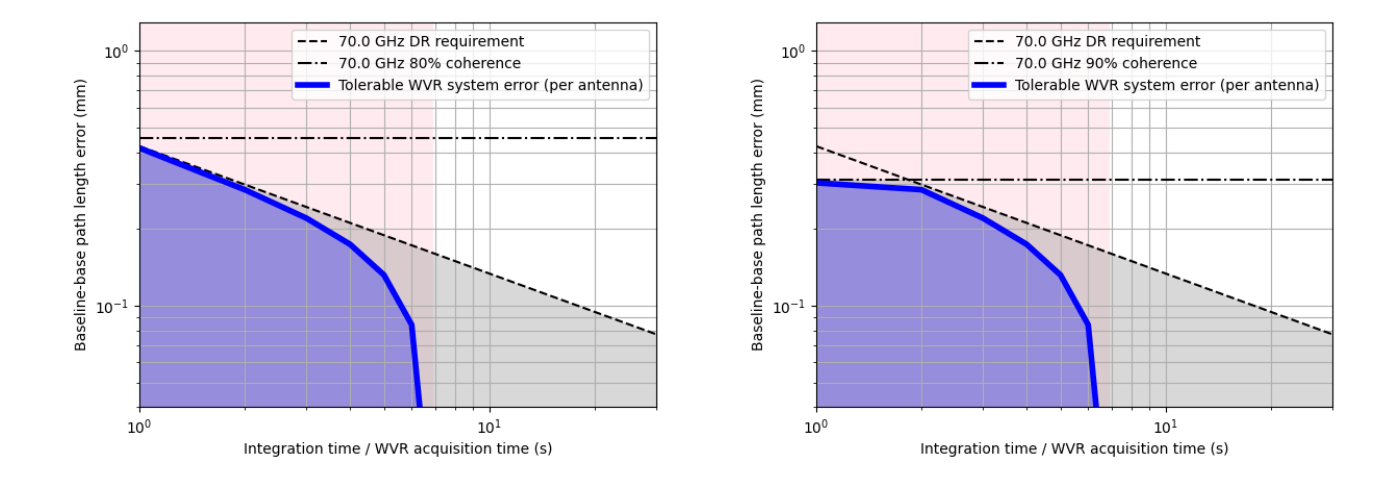


Figure 5. The same as Figure 4 but DR requirement of 30 dB at 70 GHz in Band 6.

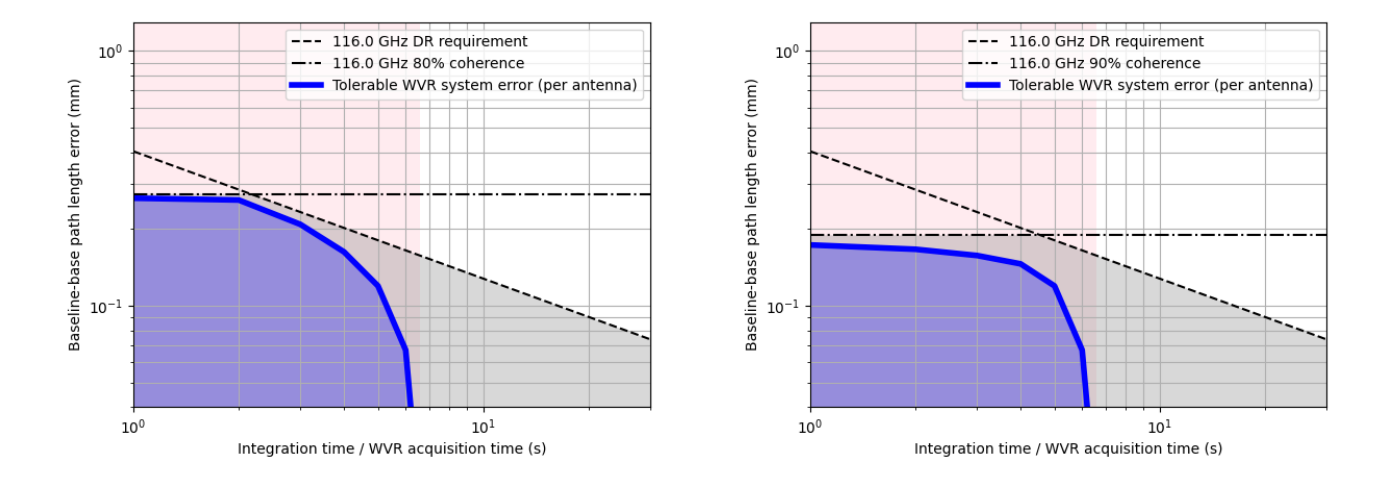


Figure 6. The same as Figure 4 but DR requirement of 28 dB at 116 GHz in Band 6.

Table 2. Tolerable WVR system error ($\sigma_{\rm wvr}$ in path length and PWV) for $t_{\rm wvr}$ of 1, 2, 3 and 4 s and for $\eta_{\rm c}$ of 80% and 90%

	$\eta_{\rm c}=80\%$	$\eta_{\rm c} = 90\%$		
$t_{ m wvr} = 1 \ m s$	264 μm (PWV: 41.9 μm)	173 μm (PWV: 27.5 μm)		
$t_{ m wvr} = 2 \ m s$	246 μm (PWV: 39.0 μm)	167 μ m (PWV: 26.5 μ m)		
$t_{ m wvr} = 3 \ m s$	187 μm (PWV: 29.7 μm)	157 μ m (PWV: 24.9 μ m)		
$t_{\rm wvr} = 4 { m s}$	141 μ m (PWV: 22.4 μ m)	141 μm (PWV: 22.4 μm)		

3.3. Tolerable WVR system error

Combining the DR requirement and the assumed tolerable coherence losses, the error budget for the WVR system (σ_{wvr}) should be allocated to fall in the region of overlap between the gray and pink areas in Figures 4, 5, and 6. The baseline-based error budget combining each time scale dependent WVR error component of σ_{wvr} (in Equation (15) and shown in Figure 2 and Table 1) for the worst case in the winter season (November daytime) is shown by the blue lines. For ngVLA high frequency observations, the WVR system measurement should meet this specification.

As discussed in Section 3.1, the most stringent path length error constraint from the DR requirement is given by the Band 5. However, the path length error constraint arising from the coherence goals becomes more stringent at higher observing frequencies. The coherence goals have no effect on the error tolerance at 50.5 GHz, while at 116 GHz it has the greatest impact on the error tolerance, particularly in the short t_{wvr} range (typically $t_{\text{wvr}} \leq 4$ s).

The tolerable 1- σ errors of the full WVR system, plotted as blue lines, are listed in Table 2, integrating the three cases (50.5, 70, and 116 GHz). The requirement we recommend for tolerable WVR path length error at $t_{\rm wvr}$ of 1-2 s are $\sim 160-180~\mu{\rm m}$ for 90% coherence goal and $\sim 240-270~\mu{\rm m}$ for 80% coherence goal.

3.4. Effect of residual atmospheric phase fluctuations on synthesized images using WVR phase correction + phase referencing

Carilli (2015) discusses effects of the residual atmospheric phase fluctuations on ngVLA synthesized images at 3 mm wavelength using fast switching phase referencing. Similarly, to explore how the proposed phase calibration strategy (WVR and 120 s phase referencing for wet and dry component fluctuations) performs at the highest frequencies, we conducted ngVLA observation simulations at 116 GHz using the interferometric visibility data simulator ARIS (Asaki et al. 2007).

Figure 7 shows the array configuration for the simulated ngVLA observation (Rev D Core, Carilli et al. 2021), limited to 65 antennas to conserve computational resources. We activated only atmospheric phase fluctuations as observational errors and implemented two types of atmospheric phase screens: one for WVR-corrected wet component phase fluctuations and another for the dry component phase fluctuations described in Section 2.4. For the WVR-corrected phase screen, two cases were prepared with the WVR acquisition intervals of 4 s and 10 s (longer than the recommended correction timescale, section 3.3), as shown in the bottom left panel of Figure 2. Figure 8 shows the simulated interferometric phase time series for an example baseline (cor111–cor113 illustrated in Figure 7) and the phase referencing calibrated target source phase with 120 s cycle time. Figure 8 also presents the SSF before and after phase referencing calibration for all 2080 baselines. The CLEAN images synthesized from the phase-calibrated visibility data shown in Figure 9 used uniform weighting.

One effect of the atmospheric phase fluctuations in radio interferometric observations, as discussed by Carilli (2015), is radio seeing (resolution degradation of the synthesized beam) due to the interferometric phase noise, resulting in loss of angular resolution. To estimate the beam degradation effect in this ngVLA observation simulation, we compared the CLEAN images with a phase-noise-free image. The synthesized beam size for the two CLEAN images (Figure 9) is 130×100 mas (PA= 108°) and the noise-free CLEAN image shows a 2D Gaussian component of 130×100 mas (PA= 100°), which closely matches the synthesized beam. The CLEAN images containing the phase noise have 130×100 mas (PA= 97.8°) for both the 4 s and 10 s WVR acquisition intervals. Therefore, we con-

clude that no significant degradation in the angular resolution is observed using the proposed phase calibration method, and the beam resolution degradation is not important for the ngVLA Core array. Image peak intensity degradation in the CLEAN images was also investigated: for 4 s and 10 s WVR acquisition intervals, the values are 0.967 and 0.939 Jy beam⁻¹, respectively, while the maximum value for the noise-free CLEAN image is 1 Jy beam⁻¹. A trend of decreasing peak intensity is observed as the WVR acquisition interval increases. This degradation stems from coherence loss due to the residual atmospheric phase fluctuations. The impact of this coherence loss can be mitigated by adopting shorter WVR acquisition intervals.

Calculating the tolerable WVR system error $\sigma_{\rm wvr}$ using the image peak values obtained from the simulation results for the 4 s WVR acquisition interval yields 365 and 271 μ m for the 80% and 90% coherence requirements, respectively. In contrast, the analytical study indicates 163 and 146 μ m for the 80% and 90% coherence requirements (Table 2). This discrepancy is considered to stem from the baseline length dependence of the residual atmospheric phase error as shown with the blue cross marks in the bottom left panel of Figure 8. For arrays containing short baselines of tens to hundreds meters, $\sigma_{\Delta\Phi_{\rm d}}$ is smaller: however, the analytical study assumes all baselines have the same $\sigma_{\Delta\Phi_{\rm d}}$ corresponding to 8 km, conservatively, as discussed in Section 3.1. If imaging simulations are performed on larger arrays excluding such short baselines, the tolerable WVR system error obtained from the simulation study is expected to approach the values listed in Table 2.

Table 3. General observation parameters in imaging simulation with residual atmospheric phase fluctuations

Item	Value		
Array configuration	65 antennas from Rev D Core (Carilli et al. 2021)		
Observation time	Jan 20, 00:00:00 - 03:00:00 UTC		
Observation frequency	116 GHz		
Target source	$(RA, Dec) = (03^{h}00^{m}00^{s}.0, 45^{\circ}00'00''.0) (1 Jy)$		
Phase calibrator	2° separated from the target to the north (1 Jy)		
Cycle time	120 s (80% duty ratio for the target source)		
Atmospheric phase fluctuations	Figure 2 bottom left panel		
Wind speed	$7.6 \text{ m s}^{-1} \text{ (west wind)}$		

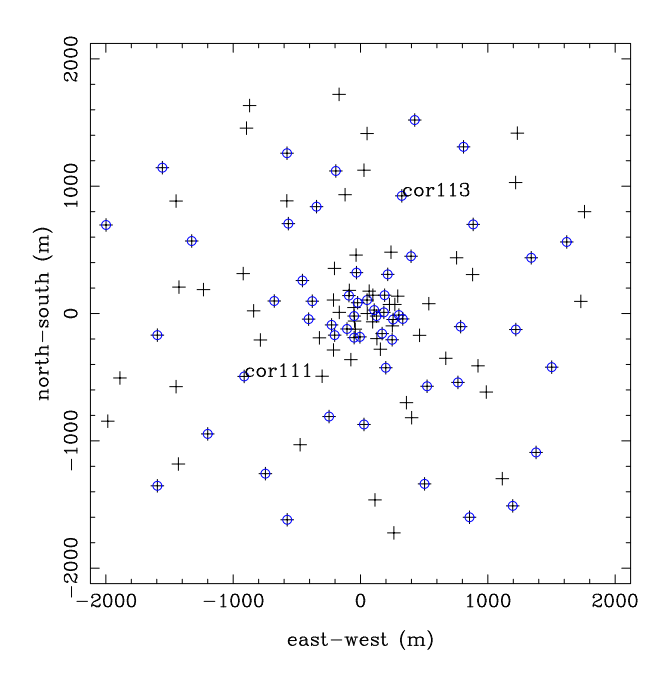


Figure 7. Antenna configuration of the imaging simulation. Cross marks represent antenna positions in Rev D Core (Carilli et al. 2021). Blue open circles represent antennas assumed participate in the simulated observations.

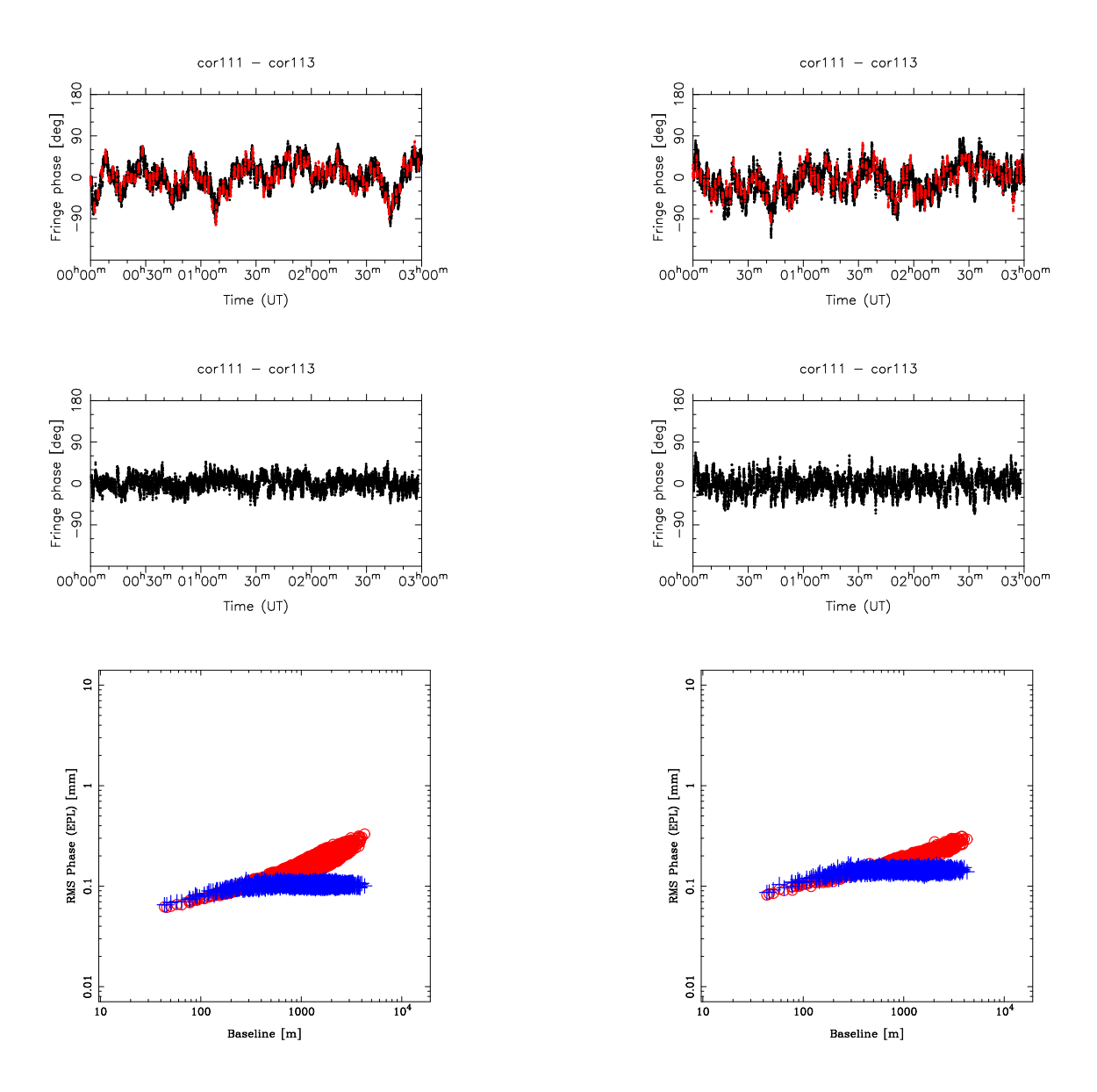
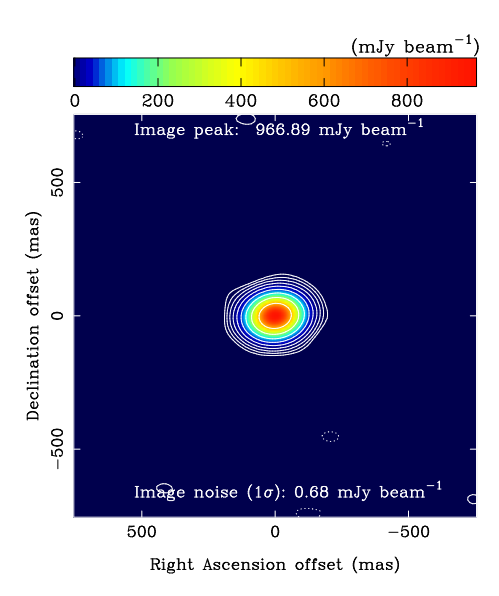


Figure 8. Example of ngVLA interferometric phase time series and SSF at 116 GHz from simulation. Top: WVR-corrected interferometric phase between cor111 and cor113 as illustrated in Figure 7. Black and red dots represent interferometric phases for the target source and phase calibrator, respectively. Cross correlation is assumed to be made every second. Middle: target source phase calibrated with the 120 s cycle time phase referencing. Bottom: SSF before and after phase referencing shown by the red open circles and blue crosses, respectively. The left and right panels show WVR acquisition intervals of 4 s and 10 s, respectively.



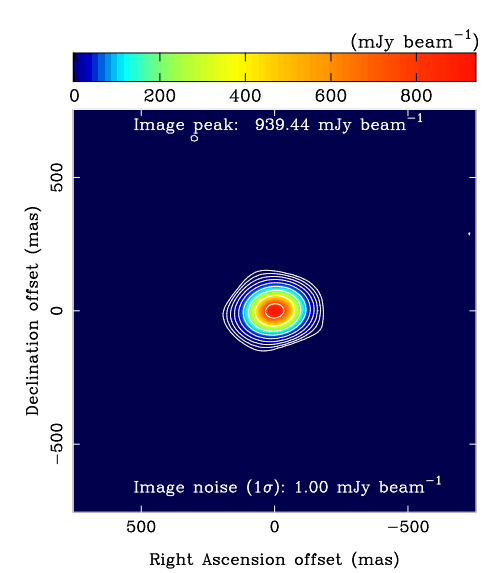


Figure 9. CLEAN images synthesized from the simulated visibility data using uniform weighting. Left: 4 s WVR acquisition interval. Right: 10 s WVR acquisition interval. Contour levels start from 3σ (image rms noise). The image peak intensity is shown at the top of the panel, and the image rms noise is shown at the bottom. The synthesized beam is 130×100 mas (PA= 108°).

4. FUTURE WORK: ERROR BUDGET WITHIN THE WVR SYSTEM

The WVR system consists of a hardware subsystem and a path length (or delay) retrieval algorithm (modeling software) subsystem. The hardware subsystem contributes a water line brightness temperature measurement error due to the system noise and instability and the algorithm subsystem contributes a modeling calculation error in obtaining the refractive index of the 22 GHz atmospheric water line. The former depends on the stability of the WVR front end, the receiver's noise temperature, the received bandwidth, and the calibration system. The latter depends on the frequency coverage and channelization spacing, the calculation model and algorithm, and the fitting parameters, such as the weight for each channel. In this initial study, we have not assumed a specific WVR system implementation e.g., a standalone WVR system or a standard ngVLA Band-4 science receiver based WVR system, the number of channels, filtering bandwidth, center frequencies of the channels, or the details of the algorithm. These are being separately pursued (Sridharan et al. (2025), Massingil et al, 2026, in preparation). An investigation of the error budget allocation break down between the WVR hardware and software subsystems is necessary to determine the specifications and design of these WVR subsystems (e.g., Butler 1999), whose combination should meet the overall WVR system requirement derived here.

5. CONCLUSIONS

We have studied the overall requirements for a prospective ngVLA WVR system to correct for tropospheric delay fluctuations. A statistical model incorporating a spatial phase structure function, whose parameters are anchored by results from the VLA site testing interferometer with monthly and day/night granularity, formed the basis of the study. We studied the performance of fast switching reference calibration as a simple example, showing a small impact for a 2° target-calibrator angular separation. The statistical model framework was applied to water vapor radiometry based corrections to derive residual fluctuations for a range of time scales and baselines. The impact of dry air fluctuations, which cannot be corrected for by a WVR, was also treated in a simple model, suggesting fast switching reference calibration as the mitigation strategy, if necessary, for long baselines. Combining

ngVLA dynamic range requirements in Bands 5 and 6 and assumed limits to amplitude loss due to decoherence, for which there are no ngVLA requirements, the allowable region in the timescale - path length error parameter space for the overall WVR system was identified. The resulting requirements recommended for the overall ngVLA WVR system for 1-2 s sampling rate are path length errors of $\sim 160-180~\mu m$ for 90% coherence goal and $\sim 240-270~\mu m$ for 80% coherence goal. Future work is needed to break down and allocate this requirement to the hardware and software subsystems of the WVR, for water vapor sensing and path length estimation respectively, and to develop these subsystems. We also studied possible degradation of the resolution of the synthesized beam due to residual fluctuations after correction for the ngVLA Core array and found it to be not important.

APPENDIX

A. STANDARD DEVIATION OF A TWO ELEMENT INTERFEROMETRIC PHASE

Let us explain how to obtain the standard deviation σ_{Φ} of a two element interferometric phase Φ from structure functions by following the discussions described by Asaki et al. (1996). The standard deviation σ_{Φ} is expressed as follows:

$$\sigma_{\Phi}^{2} = \left\langle \frac{1}{t_{\text{obs}}} \int_{0}^{t_{\text{obs}}} \left\{ \Phi(t) - \frac{1}{t_{\text{obs}}} \int_{0}^{t_{\text{obs}}} \Phi(t') dt' \right\}^{2} dt \right\rangle
= \frac{1}{t_{\text{obs}}} \int_{0}^{t_{\text{obs}}} R_{\Phi}(0) dt - \frac{1}{t_{\text{obs}}^{2}} \int_{t=0}^{t=t_{\text{obs}}} \int_{t'=0}^{t'=t_{\text{obs}}} \left\langle \Phi(t) \Phi(t') \right\rangle dt' dt
= \frac{1}{t_{\text{obs}}} \int_{0}^{t_{\text{obs}}} R_{\Phi}(0) dt - \frac{1}{t_{\text{obs}}^{2}} \int_{t=0}^{t=t_{\text{obs}}} \int_{t'=0}^{t'=t_{\text{obs}}} R_{\Phi}(t-t') dt' dt,$$
(A1)

where t_{obs} is the observation time, and $R_{\Phi}(\Delta t)$ is an auto correlation function of $\Phi(t)$ with a time lag of Δt . Introducing a variable transformation $t - t' = t'' = -\tau$ in the second term of the right side of Equation (A1) and noting $R_{\Phi}(-\tau) = R_{\Phi}(\tau)$, we obtain:

$$\frac{1}{t_{\text{obs}}^{2}} \int_{t=0}^{t=t_{\text{obs}}} \int_{t'=0}^{t'=t_{\text{obs}}} R_{\Phi}(t-t')dt'dt = \frac{1}{t_{\text{obs}}^{2}} \int_{t=0}^{t=t_{\text{obs}}} \int_{t''=t}^{t''=t-t_{\text{obs}}} R_{\Phi}(t'')(-dt'')dt
= \frac{1}{t_{\text{obs}}^{2}} \int_{t=0}^{t=t_{\text{obs}}} \int_{\tau=-t}^{\tau=-t+t_{\text{obs}}} R_{\Phi}(-\tau)d\tau dt
= \frac{1}{t_{\text{obs}}^{2}} \int_{\tau=-t_{\text{obs}}}^{\tau=0} \int_{t=-\tau}^{t=t_{\text{obs}}} R_{\Phi}(\tau)dt d\tau
+ \frac{1}{t_{\text{obs}}^{2}} \int_{\tau=0}^{\tau=t_{\text{obs}}} \int_{t=0}^{t=t_{\text{obs}}-\tau} R_{\Phi}(\tau)d\tau d\tau
= \frac{1}{t_{\text{obs}}^{2}} \int_{\tau=-t_{\text{obs}}}^{\tau=0} (t_{\text{obs}} + \tau) R_{\Phi}(\tau)d\tau
+ \frac{1}{t_{\text{obs}}^{2}} \int_{\tau=0}^{\tau=t_{\text{obs}}} (t_{\text{obs}} - \tau) R_{\Phi}(\tau)d\tau
= \frac{2}{t_{\text{obs}}^{2}} \int_{0}^{t_{\text{obs}}} (t_{\text{obs}} - \tau) R_{\Phi}(\tau)d\tau. \tag{A2}$$

On the other hand, the first term of the right side of Equation (A1) can be transformed as follows:

$$\frac{1}{t_{\text{obs}}} \int_{0}^{t_{\text{obs}}} R_{\Phi}(0) dt = \frac{2}{t_{\text{obs}}^{2}} \int_{0}^{t_{\text{obs}}} (t_{\text{obs}} - \tau) R_{\Phi}(0) d\tau.$$
 (A3)

Equations (A2) and (A3) are substituted into Equation (A1):

$$\sigma_{\Phi}^{2} = \frac{2}{t_{\text{obs}}^{2}} \int_{0}^{t_{\text{obs}}} (t_{\text{obs}} - \tau) R_{\Phi}(0) d\tau - \frac{2}{t_{\text{obs}}^{2}} \int_{0}^{t_{\text{obs}}} (t_{\text{obs}} - \tau) R_{\Phi}(\tau) d\tau
= \frac{1}{t_{\text{obs}}^{2}} \int_{0}^{t_{\text{obs}}} (t_{\text{obs}} - \tau) [2R_{\Phi}(0) - 2R_{\Phi}(\tau)] d\tau
= \frac{1}{t_{\text{obs}}^{2}} \int_{0}^{t_{\text{obs}}} (t_{\text{obs}} - \tau) \bar{D}_{\Phi}(\tau) d\tau,$$
(A4)

where $\bar{D}_{\Phi}(\tau) = 2R_{\Phi}(0) - 2R_{\Phi}(\tau)$ is a temporal structure function of two-element interferometer.

REFERENCES

Asaki, Y. 1997, PhD thesis, Graduated University of Advanced Studies, Japan

Asaki, Y., Saito, M., Kawabe, R., Morita, K.-I., & Sasao, T. 1996, Radio Science, 31, 1615, doi: 10.1029/96RS02629

Asaki, Y., Sudou, H., Kono, Y., et al. 2007, PASJ, 59, 397, doi: 10.1093/pasj/59.2.397

Asaki, Y., Matsushita, S., Fomalont, E. B., et al. 2016, in Society of Photo-Optical Instrumentation Engineers (SPIE) Conference Series, Vol. 9906, Ground-based and Airborne Telescopes VI, ed. H. J. Hall, R. Gilmozzi, & H. K. Marshall, 99065U, doi: 10.1117/12.2232301

Butler, B. 1999, VLA Scientific Memo, 177, 1
 Butler, B., & Desai, K. 1999, VLA Test Memo, 222, 1

Butler, B. J. 2020, ngVLA Memo, 73, 1 Carilli, C. L. 2015, ngVLA Memo, 1, 1

- Carilli, C. L., & Holdaway, M. A. 1999, Radio Science, 34, 817, doi: 10.1029/1999RS900048
- Carilli, C. L., Mason, B., Rosero, V., et al. 2021, ngVLA Memo, 92, 21
- Clarke, B. 2015, ngVLA Memo
- Hales, C. A. 2020, ngVLA Memo, 61, 1
- Matsushita, S., Asaki, Y., Fomalont, E. B., et al. 2017, PASP, 129, 035004, doi: 10.1088/1538-3873/aa5787
- Maud, L. T., Pérez-Sánchez, A. F., Asaki, Y., et al. 2023, arXiv e-prints, arXiv:2304.08318, doi: 10.48550/arXiv.2304.08318
- Maud, L. T., Tilanus, R. P. J., van Kempen,T. A., et al. 2017, A&A, 605, A121,doi: 10.1051/0004-6361/201731197

- Nikolic, B., Bolton, R. C., Graves, S. F., Hills,
 R. E., & Richer, J. S. 2013, A&A, 552, A104,
 doi: 10.1051/0004-6361/201220987
- Selina, R. e. a. 2021, 020.10.15.10.00-0003-REQSridharan, T. K., & Bhatnagar, S. 2023, ngVLAMemo, 108, 1
- Sridharan, T. K., Lehmensiek, R., & Asaki, Y. 2025, ngVLA Memo, 136
- Sridharan, T. K., Bhatnagar, S., Asaki, Y., et al. 2024, 020.10.05.05.00-0015 PLA
- Tatarski, V. I., Silverman, R. A., & Chako, N. 1961, Physics Today, 14, 46, doi: 10.1063/1.3057286
- Thompson, A. R., Moran, J. M., & Swenson, George W., J. 2017, Interferometry and Synthesis in Radio Astronomy, 3rd Edition, doi: 10.1007/978-3-319-44431-4
- Towne, N. 2020, ngVLA Memo Wrobel, J. M., & Ho, A. 2022, ngVLA Memo, 98,